Journal of Biomechanics 85 (2019) 27–36

Contents lists available at ScienceDirect

Journal of Biomechanics

journal homepage: www.elsevier.com/locate/jbiomech
www.JBiomech.com

An image-based kinematic model of the tibiotalar and subtalar joints and its application to gait analysis in children with Juvenile Idiopathic Arthritis

Erica Montefiori [a,*], Luca Modenese [a], Roberto Di Marco [b], Silvia Magni-Manzoni [c], Clara Malattia [d], Maurizio Petrarca [e], Anna Ronchetti [f], Laura Tanturri de Horatio [g], Pieter van Dijkhuizen [h], Anqi Wang [i], Stefan Wesarg [i], Marco Viceconti [a], Claudia Mazzà [a], for the MD-PAEDIGREE Consortium

[a] Department of Mechanical Engineering and INSIGNEO Institute for in silico Medicine, University of Sheffield, Sheffield, United Kingdom
[b] Department of Mechanical and Aerospace Engineering, "Sapienza" University of Rome, Rome, Italy
[c] Pediatric Rheumatology Unit, IRCCS "Bambino Gesù" Children's Hospital, Passoscuro, Rome, Italy
[d] Pediatria II – Reumatologia, Istituto Giannina Gaslini, Genoa, Italy
[e] Movement Analysis and Robotics Laboratory (MARLab), Neurorehabilitation Units, IRCCS "Bambino Gesù" Children's Hospital, Passoscuro, Rome, Italy
[f] UOC Medicina Fisica e Riabilitazione, IRCCS Istituto Giannina Gaslini, Genoa, Italy
[g] Department of Imaging, IRCCS "Bambino Gesù" Children's Hospital, Passoscuro, Rome, Italy
[h] Paediatric Immunology, University Medical Centre Utrecht, Wilhelmina Children's Hospital, Utrecht, the Netherlands
[i] Visual Healthcare Technologies, Fraunhofer IGD, Darmstadt, Germany

ARTICLE INFO

Article history:
Accepted 28 December 2018

Keywords:
Biomechanics
Ankle joint axis
Musculoskeletal modelling
Gait analysis
Patient-specific modelling

ABSTRACT

In vivo estimates of tibiotalar and the subtalar joint kinematics can unveil unique information about gait biomechanics, especially in the presence of musculoskeletal disorders affecting the foot and ankle complex. Previous literature investigated the ankle kinematics on *ex vivo* data sets, but little has been reported for natural walking, and even less for pathological and juvenile populations. This paper proposes an MRI-based morphological fitting methodology for the personalised definition of the tibiotalar and the subtalar joint axes during gait, and investigated its application to characterise the ankle kinematics in twenty patients affected by Juvenile Idiopathic Arthritis (JIA). The estimated joint axes were in line with *in vivo* and *ex vivo* literature data and joint kinematics variation subsequent to inter-operator variability was in the order of 1°. The model allowed to investigate, for the first time in patients with JIA, the functional response to joint impairment. The joint kinematics highlighted changes over time that were consistent with changes in the patient's clinical pattern and notably varied from patient to patient. The heterogeneous and patient-specific nature of the effects of JIA was confirmed by the absence of a correlation between a semi-quantitative MRI-based impairment score and a variety of investigated joint kinematics indexes. In conclusion, this study showed the feasibility of using MRI and morphological fitting to identify the tibiotalar and subtalar joint axes in a non-invasive patient-specific manner. The proposed methodology represents an innovative and reliable approach to the analysis of the ankle joint kinematics in pathological juvenile populations.

1. Introduction

Functional anatomy literature describes the ankle joint as a very complex structure allowing for multiple movements due to the combination of various mechanically coupled joints, including the tibiotalar (i.e. between tibia and talus) and subtalar (i.e. between talus and calcaneus) joints (Hicks et al., 1953; Siegler et al., 1988; Dettwyler et al., 2004). The biomechanical behaviour of the ankle during locomotion and its relationship with the anatomy have been investigated since the beginning of the last century (Fick, 1911; Manter, 1941; Barnett and Napier, 1952; Isman and Inman, 1969; Inman, 1976) and many authors have also estimated the kinematics of the tibiotalar and subtalar joints *ex vivo* (Hicks et al., 1953; Rasmussen and Tovborg-Jensen, 1982; van Langelaan, 1983; Siegler et al., 1988). The possibility of estimating

* Corresponding author at: Room C+13 – INSIGNEO Institute for in silico Medicine, The University of Sheffield, The Pam Liversidge Building, Mappin Street, Sheffield, United Kingdom.
E-mail address: e.montefiori@sheffield.ac.uk (E. Montefiori).

https://doi.org/10.1016/j.jbiomech.2018.12.041
0021-9290/

the kinematics of the ankle's intrinsic joints from *in vivo* data is of interest when investigating musculoskeletal diseases. Nonetheless, a comprehensive understanding of the joint's intrinsic movement during walking is still lacking. This is because measuring the motion associated to foot inversion/eversion is not trivial and most literature has focused on the quantification of articular range of motion (ROM) for the various joint's degrees of freedom (DOFs) under controlled conditions (Lundberg et al., 1989; Mattingly et al., 2006; Lewis et al., 2009).

In vivo tracking of the relative movement of the talus relative to the calcaneus using skin markers and a standard gait analysis technique is complicated by the small size of these bones and the absence of visible superficial landmarks (Scott et al., 1991; Di Marco et al., 2016). Few studies have investigated the kinematics of the intrinsic joints of the ankle during walking and running (Arndt et al., 2004, 2006) using intracortical bone pins, and compared the results to those from using superficial markers (Westblad et al., 2002). These studies clearly showed a description of plantar/dorsiflexion is possible with traditional gait analysis methods, however, estimates of inversion/eversion movement are still far from being accurate. Intracortical pin-based studies partially overcome this lack of accuracy but, due to the invasiveness of the technique, the number of participants is usually limited to few healthy volunteers, whose natural gait pattern can be altered by the possible pain and discomfort related to the implant. Both *in vivo* and *ex vivo* studies reported high intra-subject and inter-subject variability in the subtalar joint kinematics with ROM up to 60° (Roaas and Anderson, 1982; Sepic et al., 1986; Lundberg, 1989).

The functional complexity of the subtalar joint led to a number of different modelling approaches, from the attempt to capture its mobility through multi-segmental foot models where the subtalar articulation was interpreted as a motion between hind-foot and fore-foot (Prinold et al., 2016; Saraswat et al., 2010), to a more anatomical representation as a universal or hinge joint (Delp et al., 1990; Malaquias et al., 2017). The hinge-like schematisation also applies to the tibiotalar joint and this approach is currently used within widely adopted musculoskeletal models (Delp et al., 1990). When simultaneously modelling both joints as hinges (Dul and Johnson, 1985), a reasonable simplification is made with respect to their real functional role (Siegler et al., 1988), according to which the tibiotalar and subtalar joints describe the plantar/dorsiflexion and inversion/eversion motions, respectively. This latter motion, despite its simplified appearance, is justified because the predominant motion occurs about a single axis of rotation (Scott and Winter, 1991). However, this DOF has been reported to be less accurately described with current musculoskeletal modelling approaches, mainly due to the difficulties in identifying the joint functional axis *in vivo* (Van den Bogert et al., 1994; Dettwyler et al., 2004; Parr et al., 2012). A high variability within- and between-subjects has been observed in the modelled joint axes, which is also related to the specific locomotion task (Leitch et al., 2010). In the presence of musculoskeletal disorders, the adoption of image-based patient-specific modelling approaches has been previously proposed (Prinold et al., 2016; Hannah et al., 2017) and proved to increase anatomical modelling accuracy (Correa and Pandy 2011; Durkin et al., 2006; Scheys et al., 2009). The use of this technique accounts for patients' anatomical features and peculiarities, crucial when impairments and gait limitations affect the subjects. In this study, we propose an image-based modelling procedure to define the tibiotalar and subtalar joints axes, avoiding operator-dependent steps and related variability issues (Prinold et al., 2016; Hannah et al., 2017). Once compared against literature, the procedure will be used as part of a patient-specific musculoskeletal modelling approach to investigate the gait ankle kinematics in children with Juvenile Idiopathic Arthritis (JIA), a paediatric group of diseases of unknown aetiology characterised by joint inflammation potentially leading to cartilage damage. Altered gait patterns and physical disabilities (Ravelli and Martini, 2007) are possible outcomes in JIA. This longitudinal study will prove whether our modelling approach is capable of detecting clinical changes observed in the tibiotalar and the subtalar joint functions and quantify for the first time the relationship between these changes and the underlying joint impairments.

2. Methods

2.1. Subjects and data acquisition

Twenty participants (5 males, 15 females, age: 11.6 ± 3.1 years, mass: 47.6 ± 18.2 kg, height: 148 ± 17 cm, 11 new onsets) affected by Juvenile Idiopathic Arthritis (JIA) of various sub-types (oligoarticular onset JIA, polyarticular JIA, psoriatic arthritis, and undifferentiated arthritis) (Ravelli and Martini, 2007) were recruited among those referred to two different children's hospitals (Istituto Giannina Gaslini, Genoa (Lab 1), and "Bambino Gesù" Children's Hospital, Rome (Lab 2)). The study was conducted following Helsinki's declaration on human rights and was approved by the ethical committee of both hospitals. Written informed consent was obtained by patients' parents.

Medical resonance images (MRI) and gait analysis data were collected at three time-points (6 months apart) to follow the disease progression. The imaging performed at month 0 (M0) and month 12 (M12) included a foot and ankle regional MRI (multi-slice multi-echo 3D Gradient Echo (mFFE) with water-only selection (WATS) with 0.5 mm in-plane resolution and 1 mm slice thickness). The month 6 (M6) imaging included a full lower limb MRI (3D T1-weighted fat-suppression sequence (e-THRIVE) with 1 mm in-plane resolution and 1 mm slice thickness). The core set of basic sequences and definitions suggested by the Outcome Measure in Rheumatology (OMERACT) MRI Working Group (Ostergaard et al., 2003; Nusman et al., 2016) was used to provide an MRI-based evaluation of the joints (Table 1). A weighted, average index (I_{MRI}) was used to quantify the overall level of impairment of the foot and ankle region.

Gait analysis was based on stereophotogrammetry and data were collected using a 6-camera system (BTS, Smart DX, 100 Hz) with two force plates (Kistler, 1 kHz) in Lab 1, and an 8-camera system (Vicon, MX, 200 Hz) and two force plates (AMTI, OR6, 1 kHz) in Lab 2. Five walking trials at self-selected speed were performed and a minimum of three trials were used for the analysis. The marker set included forty-four markers from the Vicon Plug in gait protocol (Vicon Motion System) and the modified Oxford Foot Model (mOFM) protocol (Stebbins et al., 2006). A subset of MRI-visible markers (twenty-eight in the lower limb MRI and six in the regional MRI scans) was retained during the imaging acquisition for data registration. Despite being collected in different centres and with different equipment, the raw-data underwent the same pre-processing in terms of labelling, gap-filling (spline algorithm built in Vicon Nexus 1.8.5 (Woltring et al., 1986)), and smoothing (4th-order Butterworth filter, 6 Hz cut-off (Barlett et al., 2007)).

2.2. Anatomical model

A statistical shape modelling approach (Steger et al., 2012) was used to segment the lower limb bones from the MRI and subject-specific anatomical models were produced using specialised software (NMSBuilder, Valente et al., 2017). For each patient, two bilateral three-segment anatomical models were built using the M0 and M12 datasets, resulting in 80 foot models. Twelve of these were excluded due to incompleteness of the experimental dataset,

Table 1
MRI scoring.

Index	MRI sequence	Scale	Sites
Bone erosion	T1-weighted fat-saturated	Range 0–10 % of eroded articular surface (Ostergaard et al., 2003) 0 = no erosion; 1 = 1–10%; 2 = 11–20%; 3 = 21–30%; 4 = 31–40%; 5 = 41–50%; 6 = 51–60%; 7 = 61–70%; 8 = 61–80%; 9 = 81–90%; 10 = 91–100%	Distal tibial epiphysis Distal fibula epiphysis Tarsal bones Metatarsal bases
Cartilage damage	WATS	Range 0–3 % of damaged cartilage surface 0 = no damage; 1 = 1–33%; 2 = 34–66%; 3 = 67–100%; 4 = extensive damage causing ankyloses	Tibiotalar Between distal talus and calcaneus, Talonavicular Calcaneocuboid Cuneonavicular Between cuneiforms and I, II and III metatarsal bones Between cuboid and IV and V metatarsal bones
Synovitis	T1-weighted fat-saturated	Range 0–3 Degree of synovial enhancement and synovial thickness (Ostergaard et al., 2003; Malattia et al., 2011) 0 = normal; 1 = mild; 2 = moderate; 3 = severe	Tibio-peroneo-talar Subtalar Talonavicular Calcaneocuboid I-V tarsometatarsal Cuneonavicular
Tenosynovitis	T1-weighted fat-saturated with enhancement	Range 0–3 Degree of peritendinous effusion or synovial proliferation 0 = normal; 1 = mild (less than2 mm); 2 = moderate (2–5 mm); 3 = severe (>5 mm)	Anterior tibial Extensor digitorum longus Extensor hallucis longus Posterior tibial Flexor digitorum longus Flexor hallucis longus Peroneal tendons

resulting in a final dataset of 68 feet. The joints' reference frames, namely tibiotalar joint (between tibia and talus) and subtalar (between talus and foot) were defined according to the ISB conventions (Baker et al., 2003) and the joint axes were identified through morphological fitting of articular surfaces (Fig. 1A-C). The subtalar joint axis (*SubAxis*) was defined as the axis connecting the centres of the spheres fitted to the anterior (Talonavicular sphere) and to the posterior-inferior (*Talocalcaneal sphere*) facets of the talus respectively (Fig. 1B). This was similar to that proposed by Parr et al., 2012, who, however, used the anterior-inferior portion of the talus surface to define the Talonavicular sphere. To define the tibiotalar joint axis (*TibAxis*), a cylinder was fitted to the entire trochlea (*Talartrochlea cylinder*) as a simplification of the approach proposed by Siegler et al., 2014 (Modenese et al., 2018). The fitting was implemented in Meshlab (Cignoni et al., 2008) by identifying the articular surfaces from the segmented geometries and minimising the least squares distance between the identified surface and the corresponding best fitting analytical shape (Least Squares Geometric Elements library, Matlab). The distal tibia (segmented from the M0/12 MRI) was afterwards registered to the entire tibia (M6 dataset) using the Iterative Closest Point algorithm in Meshlab to obtain a full lower limb model. A comprehensive description of the modelling procedure is available as supplementary material in Modenese el al. (2018). The data and models presented in this paper are available on Figshare (doi: https://doi.org/10.15131/shef.data.5863443.v1).

2.3. Joint kinematics

The OpenSim's (Delp et al., 2007) Inverse Kinematics (IK) tool was run to estimate the tibiotalar and subtalar joint angles starting from a set of sixteen skin markers (five on the tibia, eleven on the foot, Fig. 2), eight were also virtually palpated on the medical images. The difference between the virtual and experimental markers estimated by the IK tool was less than 1 cm on average over all the time-steps, as suggested in the OpenSim best practice recommendations (Hicks et al., 2015).

2.4. Model evaluation

2.4.1. Sensitivity to operator-dependent input

The bone segmentations from three randomly chosen patients were used to investigate the effect of operator-dependent variability in the definition of *TibAxis* and *SubAxis*. Three operators repeated the morphological fitting three times and the coordinates of the *Talartrochlea cylinder*, *Talocalcaneal sphere* and *Talonavicular sphere* centres were used for the comparison. A 3D quantification of their variability (SD_{3d}) was calculated from the standard deviation of the point coordinates (sd_x,sd_y,sd_z) as:

$$SD_{3d} = \sqrt{sd_x^2 + sd_y^2 + sd_z^2}$$

For the foot that led to the worst-case scenario (higher inter-operatorSD_{3d}), a second level of analysis was conducted to quantify the propagation of this error on the joint kinematics. The nine models built by the three operators were then used to estimate the tibiotalar and subtalar joint kinematics using data from one randomly selected gait trial from the same patient. The maximum value of the mean and standard deviation calculated over the nine repetitions for each point of the gait cycle was then used to quantify the maximum expected error.

2.4.2. Consistency with literature data

Among the 68 available models, 38 were selected (19 per side, preferentially from M12) to conduct the following analysis. A standing trial collected during the gait analysis session was used to identify the pose of each subject and the resulting neutral position of the foot. The transverse, sagittal, and coronal anatomical planes, the midline of the foot (*FootAxis*) and the long axis of tibia (*TibiaAxis*) were identified using the standing trial markers (Fig. 3-A-B). These allowed quantifying the tibiotalar inclination (Tib_{Incl}) and deviation (Tib_{Dev}), and the subtalar inclination (Sub_{Incl}) and deviation (Sub_{Dev}) as shown by the angles in Fig. 3C. Tib_{Incl}, Tib_{Dev}, Sub_{Incl} and Sub_{Dev} were compared to literature data from *ex vivo* cadaveric specimens (Isman and Inman, 1969; Inman, 1976) and from healthy adults (Van den Bogert et al., 1994). The estimations of *TibAxis* and *SubAxis* at M0 and M12 were also compared. All 26 models for which the 3D anatomy was available at both time-points (52 models) were used for a between-session comparison. For this analysis, the angle between the two joint axes (*InterAxis*) was preferred over the measures of Tib_{Incl}, Tib_{Dev}, Sub_{Incl}, and Sub_{Dev} to avoid the effect of experimental markers repositioning (between the two sessions) on these angles. Mean and maximum between-session variations were quantified, and a paired-two-sided

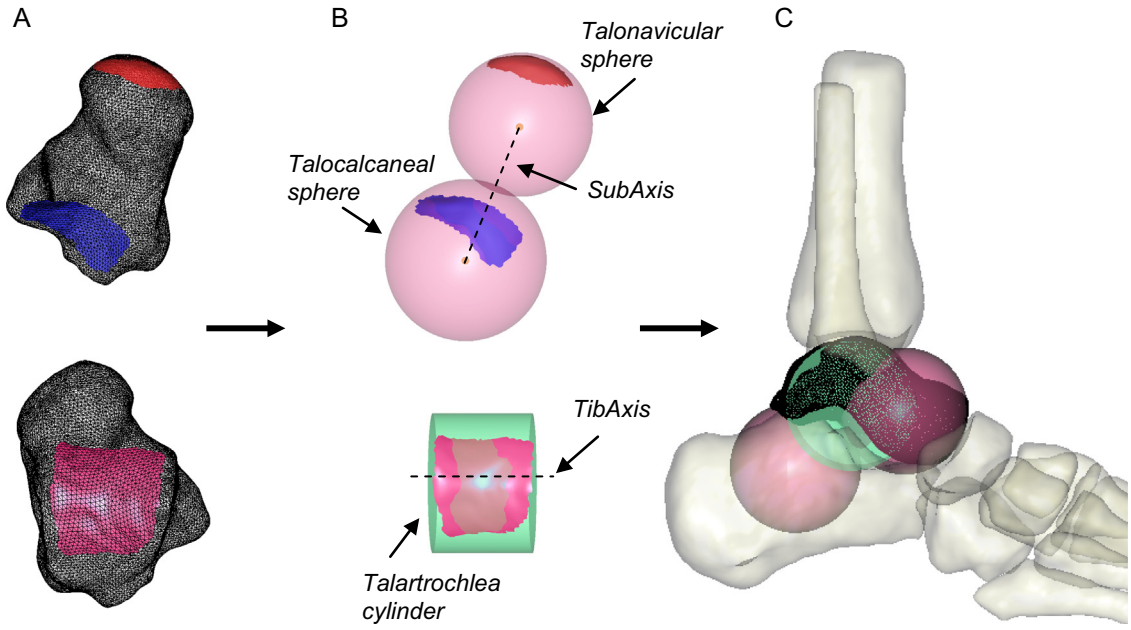

Fig. 1. (A) Plantar (top) and dorsal (bottom) views of the right talus (black wireframe) with highlighted articular regions: anterior facet (red), posterior-inferior facet (blue), trochlea (fuchsia). (B) Fitting of analytical shapes to the selected articular regions: two spheres (light pink) identify the axis of the subtalar joint (SubAxis) as the axis connecting the centres of the spheres and a cylinder (light green) identifies the axis of the tibiotalar joint (TibAxis) as the cylinder axis. (C) Example of the fitted geometries integrated within the ankle anatomical model. (For interpretation of the references to colour in this figure legend, the reader is referred to the web version of this article.)

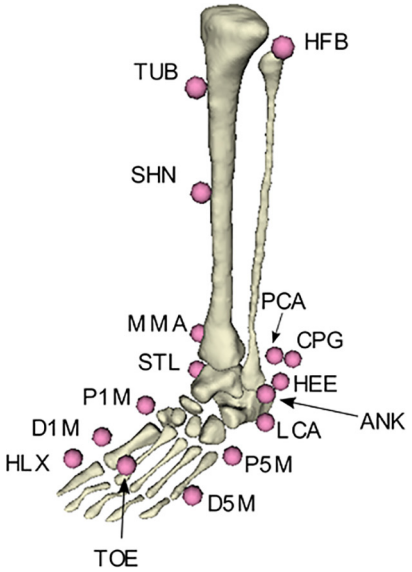

Label	Description	Markers	
		MRI	Stereo
HFB	Head of the fibula	Yes	Yes
SHN	Anterior aspect of shin	Yes	Yes
TUB	Tibial tuberosity	-	Yes
MMA	Medial malleolus	Yes	Yes
ANK	Lateral malleolus	Yes	Yes
PCA	Posterior medial aspect of heel	-	Yes
STL	Sustentaculum tali	-	Yes
LCA	Lateral calcaneus	-	Yes
CPG	Wand marker on posterior calcaneus aligned with transverse orientation	-	Yes
HEE	Posterior distal aspect of heel	-	Yes
P1M	Lateral aspect of 1st metatarsal base	-	Yes
P5M	Lateral aspect of 5th metatarsal base	-	Yes
TOE	Between 2nd and 3rd metatarsal heads	Yes	Yes
D1M	Lateral aspect of 1st metatarsal head	Yes	Yes
D5M	Lateral aspect of 5th metatarsal head	Yes	Yes
HLX	Medial side of the proximal hallux	Yes	Yes

Fig. 2. Experimental markers used in the imaging (MRI) and stereo-photogrammetric (Stereo) measurements.

Wilcoxon signed-rank test ($\alpha = 0.05$) was performed under the null hypothesis showed that no statistical difference existed between the two repeated measures. This was intended as a repeatability assessment of the proposed method, assuming in the investigated age range, and within 12 months, neither disease progression (Ravelli and Martini, 2007) nor growth (Evans, 2010) would cause changes in the joint morphology.

2.4.3. Effect of clinical impairment on joint kinematics

The models from 13 subjects (3 males, 10 females, age: 11.0 ± 3.1 years, mass: 44.5 ± 16.9 kg, height: 143 ± 13 cm, 8 new onsets), for whom both clinical and biomechanical information was available, were used to test the link between changes in the kinematics and impairment of the ankle as measured from the MRI. The I_{MRI} scores were used to classify the disability level of each

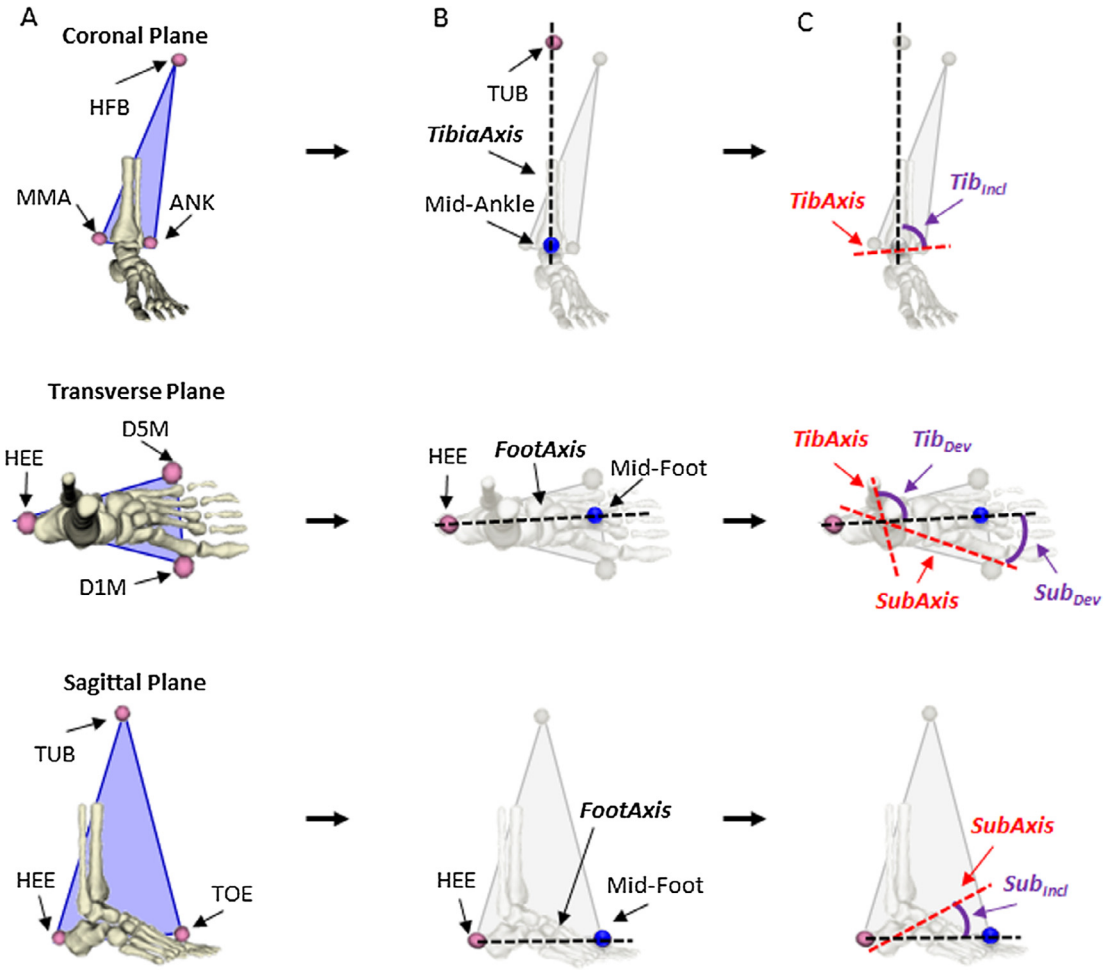

Fig. 3. (A) Identification of anatomical planes (blue triangles) as defined using the virtual markers (pink) corresponding to the experimental markers listed in Fig. 2. (B) Definition of the anatomical axes (midline of the foot = *FootAxis*, long axis of the tibia = *TibiaAxis*, black dashed lines) by calculating average points (blue markers) between virtual marker pairs (Mid-Foot = midpoint between D1M and D5M; Mid-Ankle = midpoint between ANK and MMA). (C) Quantification of the inclination (Tib_{Incl}) and deviation (Tib_{Dev}) of tibiotalar joint and inclination (Sub_{Incl}) and deviation (Sub_{Dev}) of subtalar joint as the angles (purple arches) between the anatomical axes and the joint axes (red dashed lines) as defined through morphological fitting (Fig. 1). (For interpretation of the references to colour in this figure legend, the reader is referred to the web version of this article.)

ankle and identify better and worse time-points. They were then placed into "low-involvement" and "high-involvement" groups accordingly. The joint kinematics of the two groups were then compared using a non-parametric 1D two-tailed paired *t*-test ($\alpha = 0.05$) (Nichols and Holmes, 2002) based on Statistical Parametric Mapping (SPM) in MATLAB (v9.1, R2016b, Mathworks, USA), using the SPM1D package (Pataky et al., 2012). This was chosen since the data were not normally distributed. The following kinematic parameters were also calculated to investigate the correlation with theI_{MRI}: area under the curves of the tibiotalar and subtalar joint angles, maximum plantarflexion (PF) and dorsiflexion (DF) angles, maximum inversion (Inv) and eversion (Ev) angles, and joint ROM. Furthermore, the asymmetry between the left and right foot kinematics was quantified using the Root Mean Square Deviation (RMSD) and Mean Absolute Variability (MAV) (Di Marco et al., 2018), as well as the between-side difference of ROM and standard deviations (SD). RMSD, MAV, ROM and SD were measured at the two time-points and compared using a two-sided Wilcoxon signed-rank test ($\alpha = 0.05$). The absolute difference (ΔI_{MRI}) between left and right I_{MRI} was also calculated and a correlation analysis was used to assess whether an asymmetry in the clinical score, namely higherΔI_{MRI}, corresponded to higher values of the kinematic parameters.

3. Results

3.1. Sensitivity to operator-dependent input

SD_{3d} of *Talonavicular sphere* and *Talocalcaneal sphere's* centres are reported in Table 2, as well as the resulting maximum angular variability of the *TibAxis* and *SubAxis*, whose maximum value (9.6°) was found for the inclination of *SubAxis* in patient P3. For this patient, the propagation of inter-operator variability on the articular kinematics introduced a maximum standard deviation of 0.6° and 1.3° for the tibiotalar and subtalar joints respectively, both occurring at 63% of the gait cycle.

3.2. Consistency with literature data

The residual error of the fitting algorithm (average (±SD) across the 52 models) was equal to 0.16 (±0.05) mm, 0.48 (±0.21) mm, and 0.28 (±0.11) mm for the *Talonavicular*, *Talocalcaneal*, and *Talar-trochlea* surfaces, respectively. The average (±SD) values of the measured foot angles (Tib_{Incl}, Tib_{Dev}, Sub_{Incl}, and Sub_{Dev}) (Table 3) were found to be in line with the corresponding *ex vivo* (Isman and Inman, 1969; Inman, 1976) and *in vivo* (Van den Bogert

Table 2
Inter-operator standard deviation (SD) of fitted surfaces centres and axes.

Patients	Talartrochlea center SD_{3d}[mm]	Talonavicular center SD_{3d}[mm]	Talocalcaneal center SD_{3d}[mm]	TibAxis SD [°]	SubAxis SD [°]
P1	0.4	0.4	1.4	0.6	1.7
P2	0.5	0.8	1.5	0.8	1.3
P3	0.8	2.1	5.1	2.0	5.6

et al., 1994) measurements available in the literature. The average absolute difference between the M0 and M12 measures of *Inter-Axes* was 2.2° ± 2.1°, which was not statistically significant (Wilcoxon test p = 0.648).

3.3. Effect of clinical impairment on joint kinematics

Fig. 4 shows the estimated kinematics of two subjects with different clinical scoring: patient 1 was similarly affected by the pathology at the two observations, whereas at M12 patient 2 was in total remission, as defined by Ravelli and Martini (2007). This example highlights how the models clearly capture different kinematic patterns associated with different paths of disease progression. The observation of the joint angles also clearly indicates the ability of the model to describe changes in the gait patterns happening between the two time-points, which were also confirmed by consistent changes in the walking speed (1.51 ± 0.05 m/s at M0 and 1.22 ± 0.05 m/s at M12 for subject 1; 0.83 ± 0.03 m/s at M0 and 1.20 ± 0.04 m/s at M12 for subject 2). For the whole cohort, walking speed varied from 1.01 ± 0.24 m/s at M0 to 1.12 ± 0.13 m/s at M12, and was 1.14 ± 0.17 m/s and 0.93 ± 0.33 m/s at the "low-involvement" and "high-involvement" time-points respectively, with no significant difference. Walking speed values did not correlate with the joint impairment level, as measured with the I_{MRI} (R = −0.21 and R = 0.16 at M0 and M12, respectively). Similarly, no correlation was observed between I_{MRI} and the kinematic parameters (Fig. 5). This was confirmed by the absence of a group-wise statistically significant difference between the joint kinematics of the ankles at the "low-involvement" and "high-involvement" time-points throughout the gait cycle (Fig. 6). Fig. 7 clearly shows the absence of a significant correspondence between the asymmetry of impairment (ΔI_{MRI}) and the RMSD, MAV, ΔROM and ΔSD observed at M0 and M12. However, a smaller ΔI_{MRI} at M12 was generally associated to a smaller value of the kinematics indices at that time-point, except for the ΔSD of the tibiotalar joint and the ΔROM of the subtalar joint.

4. Discussion

The aim of the study was to propose a kinematic model of the tibiotalar and subtalar joints, and to use this model to investigate the ankle joint kinematics in a group of children with JIA. The anatomical model was based on a morphological fitting approach and underwent repeatability analysis.

The procedure proved to be robust to the operator-dependent input. Even in the worst-case scenario, where the definition of the subtalar axis was associated with high inter-operator error (9.6°), the joint kinematics varied less than 1.3°. The inter-operator variability was mainly associated with the quality of the segmented images, i.e. low resolution, bias field or noise in the MRI, and to the complexity of segmenting bone tissue in young subjects, where cortical bone is not completely ossified (Evans, 2010). Nonetheless, this error was still acceptable when compared to other possible sources of variability coming from the experimental errors, such as instrumental error and marker placement error (up to 6°±2° at the toe off (Di Marco et al., 2016)), or soft tissue artefact (up to 20% of variability in the ankle kinematics (Lamberto et al., 2017)), confirming the chosen morphological fitting approach is suitable in the presence of low quality images and/or poor bone reconstructions.

An *in vivo* validation of the proposed technique was not possible within the framework of this project due to ethics constraint in the use of approaches like dual-fluoroscopy in a paediatric population. However, the comparison with *ex vivo* (Isman and Inman, 1969; Inman, 1976), and *in vivo* (Van den Bogert et al., 1994) data certainly support the validity of the technique. Previous studies (Leitch et al., 2010; Van den Bogert et al., 1994) reported the highest between-subject variabilities in the deviation angle (up to 15°); conversely, we found the biggest differences in the inclination of the subtalar axis (14°). This could be ascribed to the subtalar axis' definition relying on the identification of the anterior facet of the talus. In the youngest children, in fact, this surface can present a layer of unossified cartilage (Evans et al., 2010), which can complicate the identification of the bone contour in the MRI, consequently affecting the results of segmentation and morphological fitting.

The second goal of the study involved the application of the modelling approach as part of the clinical gait assessment of patients with JIA. The between-session repeatability showed no statistically significant difference between the measures of *Inter-Axis* at M0 and M12, confirming our hypothesis.

The observed joint kinematics reflected the heterogeneous and patient-specific nature of the pathology, which presents several sub-types, each with a specific progression (Ravelli and Martini, 2007). In fact, the individual differences (Fig. 4) were not representative of a group behaviour (Fig. 6) as a consequence of different possible evolutions of the disease. The absence of a recognisable group pattern was demonstrated by the lack of a direct relationship between a joint's clinical impairment and its kinematics.

Table 3
Inclination and deviation of tibiotalar and subtalar joint axes and comparison with published literature datasets (n = numebr of subjects).

Angle	Isman and Inman (1969) (n = 46) mean (±SD) [°]	Inman (1976) (n = 104) mean (±SD) [°]	Van den Bogert et al. (1994) (n = 14) mean (±SD) [°]	This study (n = 38) mean (±SD) [°]
Gender	NA	NA	males	30 females/8 males
Age	Adults (age not specified)	Adults (age not specified)	Adults (age not specified)	11.2 ± 3.1 years
TibIncl	80(±4)	82.7(±3.7) (*n = 107*)	85.4(±7.4)	90.7(±4.1)
TibDev	84(±7)	–	89.0(±15.1)	82.7(±7.4)
SubIncl	41(±9)	42(±9)	35.3(±4.8)	41.1(±14.1)
SubDev	23(±11)	23(±11)	18.0(±16.2)	27.0(±9.0)

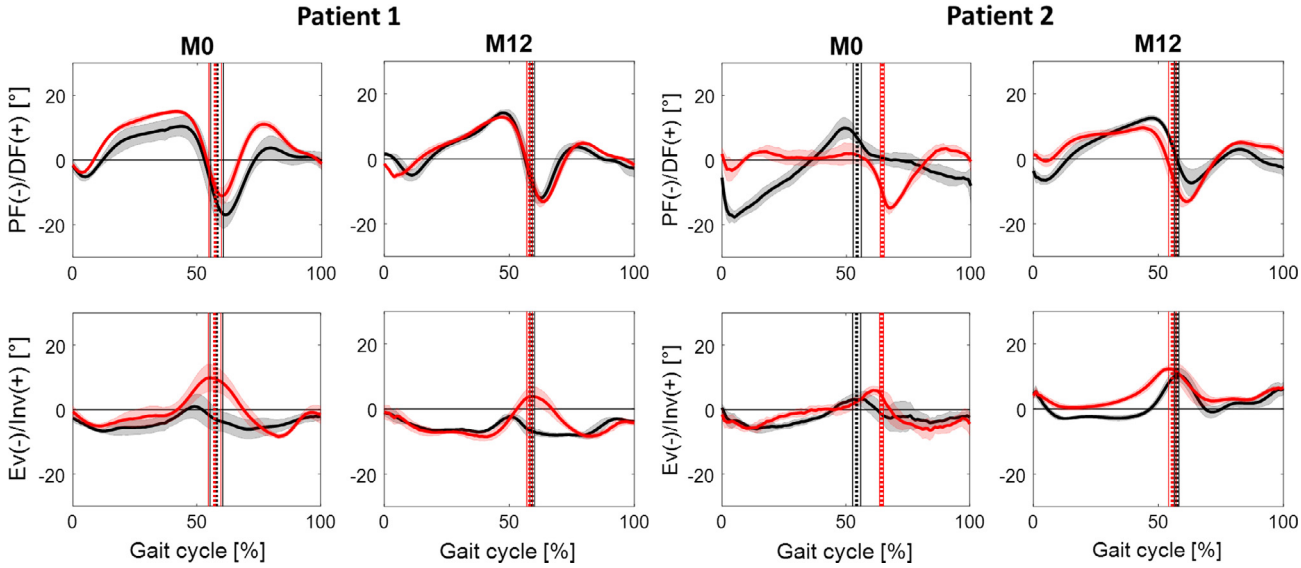

Fig. 4. Tibiotalar (PF/DF) and subtalar (Ev/Inv) joints kinematics for two JIA patients at M0 and M12. Average right (left) kinematics is shown with black (red) solid line with shadow representing ± 1 standard deviation. Toe off is shown with dotted vertical lines ± 1 standard deviation (solid vertical lines). Walking speed changed from 1.51 ± 0.05 m/s at M0 to 1.22 ± 0.05 m/s at M12 for patient 1 and from 0.83 ± 0.03 m/s at M0 and 1.20 ± 0.04 m/s at M12 for patient 2. (For interpretation of the references to colour in this figure legend, the reader is referred to the web version of this article.)

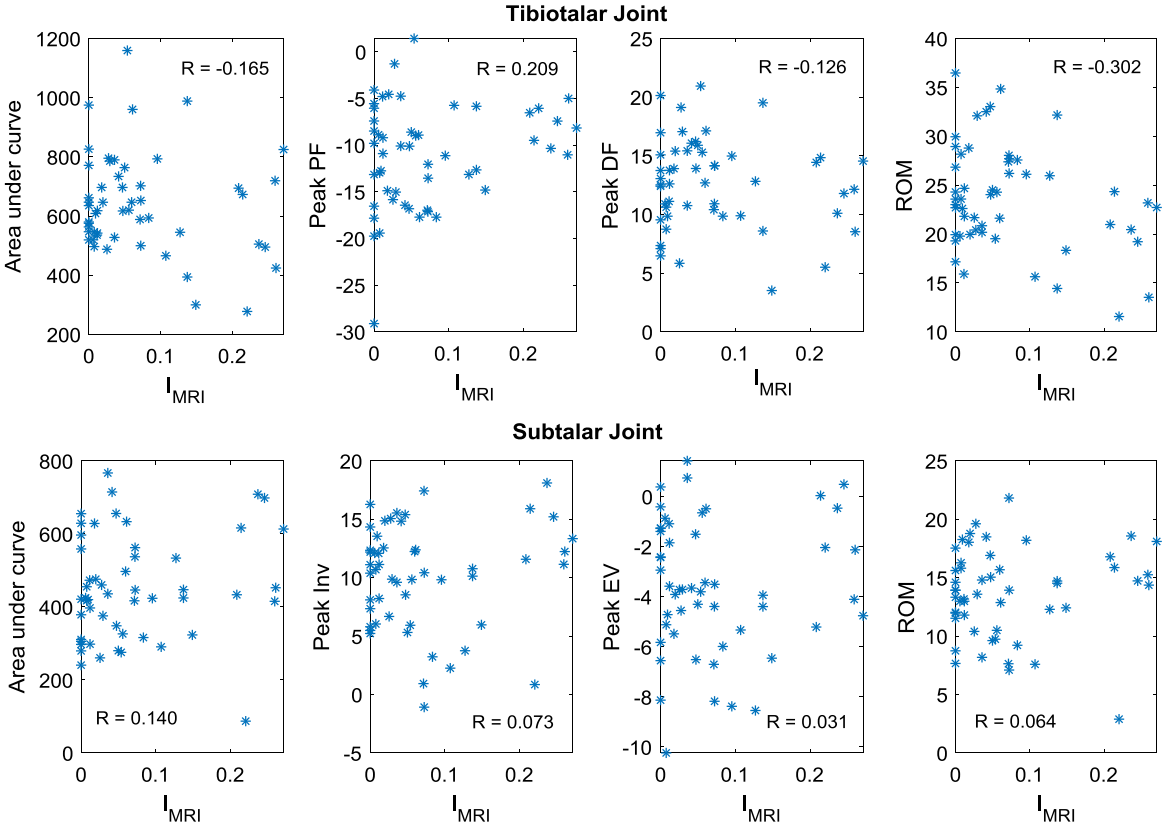

Fig. 5. Correlation between joint impairment level (I_{MRI}) and joint kinematics parameters (area under the curve, peak of plantarflexion (Peak PF) and dorsiflexion (Peak DF), peak of Inversion (Peak Inv) and eversion (Peak Ev), ROM) for all feet and observations.

The inter-subject variability was probably exacerbated by the heterogeneity of the cohort in terms of age, anthropometry, disease subtype and activity level. This explains the lack of correlation between joint kinematics (and their changes between time points) and the patient's I_{MRI} scores. This also held true for the walking speed, which was not correlated with the MRI scores, but was found in line with the 1.17 ± 0.02 m/s reported by Esbjörnsson et al. (2015) for a group of JIA children with similar ankle involvement. If group stratification needs to be pursued, then further investigation should aim at involving larger subgroups for every sub-type of JIA and matching them by age and size.

The analysis of the between-limb asymmetry at the two time-points showed similar trends in the distribution of ΔI_{MRI} and in the observed kinematics indices, despite none of the latter was

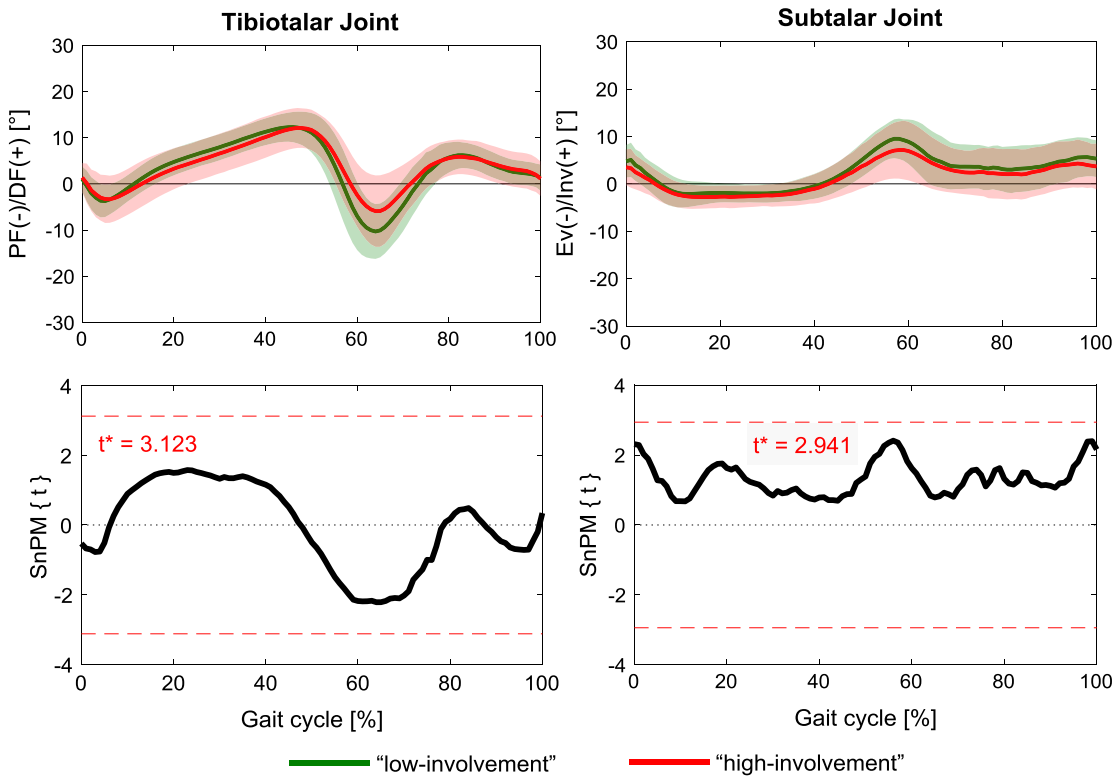

Fig. 6. Tibiotalar (PF/DF) and subtalar (Ev/Inv) joint kinematics of the 13 subjects as calculated at the "low-involvement" (green) and "high-involvement" (red) time-point. Solid lines in the left graphs represent mean values and bands represent ± 1 standard deviation. The right figures show the corresponding distribution of *t*-values (SnPM{t}) throughout the gait cycle as obtained from the non-parametric 1D paired *t*-test (Nichols and Holmes, 2002), calculated using the SPM1D package (Pataky et al., 2012). Each group includes 24 mono-lateral models (2 models were excluded from the analysis). (For interpretation of the references to colour in this figure legend, the reader is referred to the web version of this article.)

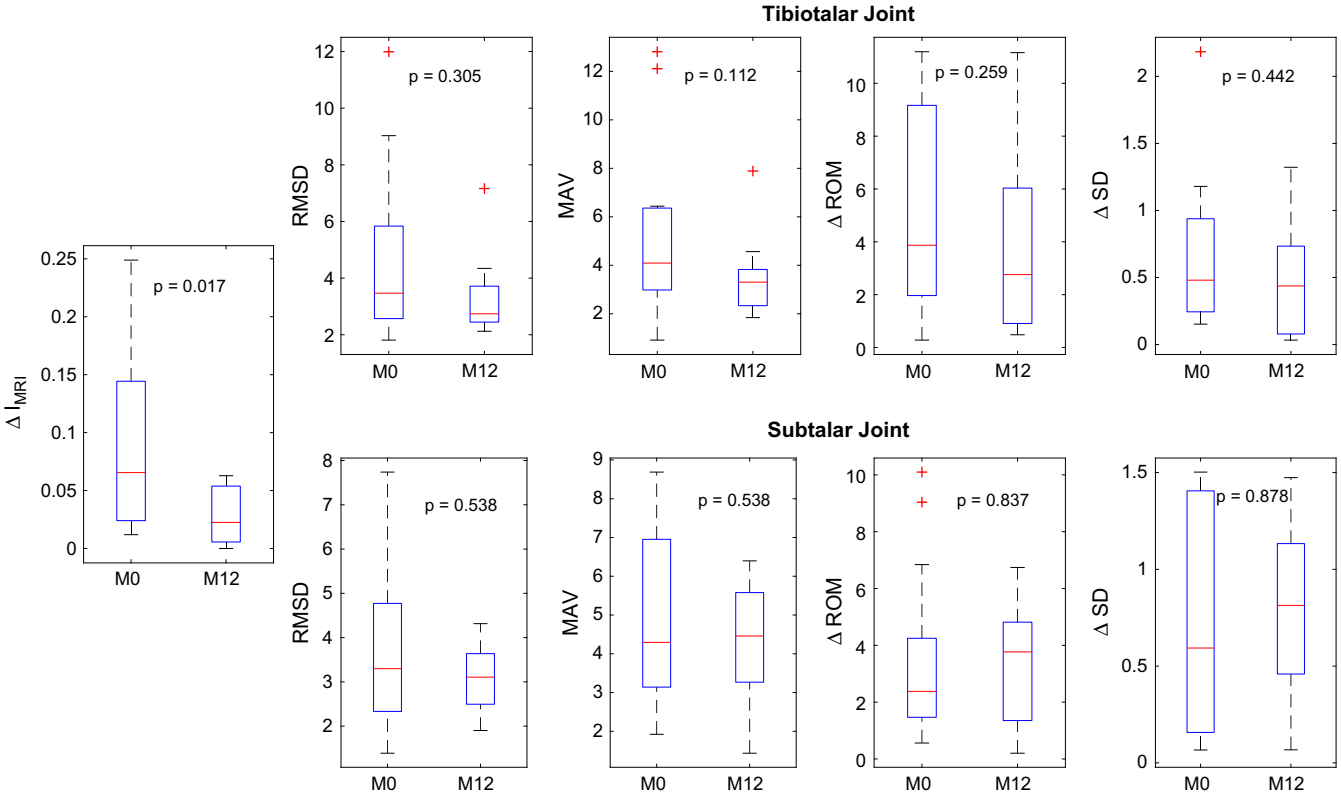

Fig. 7. Boxplot distribution of ΔI_{MRI} and kinematics indices (RMSD, MAV, ΔROM and ΔSD) for both tibiotalar and subtalar joints (n = 13) at M0 and M12. *p*-values from two-sided Wilcoxon signed-rank test are reported in each plot. Data outliers are marked with a+.

significantly different between the two time-points. In the tibiotalar articulation, lower ΔI_{MRI} at M12 corresponded to smaller RMSD and MAV, confirming the asymmetry in the clinical involvement of the ankles is reflected by an asymmetry in the biomechanics of gait. The subtalar kinematics was in general less informative and this is probably associated to a smaller ROM of this joint when compared to the tibiotalar joint, potentially resulting in smaller sensitivity to kinematics changes. Furthermore, disease-related alterations in the movement are likely to be compensated by the tibiotalar joint being dominant in the ankle kinematics (Lundberg et al., 1989) and therefore limiting the role of the subtalar joint. The lack of an independent clinical assessment of the two joints must be considered as a limitation in the study. In fact, the present work is based on the assumption that the I_{MRI} score, evaluating the overall condition of the ankle joint, is representative of both tibiotalar and subtalar impairment level. Nonetheless, a different level of involvement of the two joints could justify their different biomechanical response. Lastly, the assumption made in schematising the joints as hinge-like mechanisms represents a substantial simplification of the true articulating surfaces, potentially limiting the representation of their true 3D motion. However, the tibiotalar kinematics was only marginally affected by this modelling choice, as this movement mainly occurs in the sagittal plane (Roach et al., 2016). On the contrary, the subtalar joint might benefit from a more detailed representation and further studies are needed to investigate this aspect.

In conclusion, this study showed the feasibility of using morphological fitting of MRI-based bone segmentation to identify the tibiotalar and subtalar joint axes in a non-invasive patient-specific manner. Including these joints in a musculoskeletal model of the lower limb, coupled with an appropriate marker set, can give a better understanding of their individual contribution to the ankle biomechanics. This supports the adoption of the proposed modelling procedure into the practice of lower limb musculoskeletal modelling for the quantification of ankle biomechanics. The application to a pathological population, children with JIA, unveiled for the first time the absence of correlation between ankle impairment and biomechanical function, confirming the heterogeneous and systemic nature of this disease.

Conflict of interest

The authors declare they do not have any financial or personal relationships with other people or organizations that could have inappropriately influenced this study.

Acknowledgments

The authors want to acknowledge Dr. Norman Powell for the writing assistance. This research was supported by the European Commission (MD-PAEDIGREE project, FP7-ICT Programme, Project ID: 600932), by the UK EPSRC (Multisim project, Grant number: EP/K03877X/1) and by the NIHR Sheffield Biomedical Research Centre (BRC). The views expressed are those of the author(s) and not necessarily those of the NHS, the NIHR or the Department of Health and Social Care (DHSC).

References

Arndt, A., Westblad, P., Winson, I., Hashimoto, T., Lundberg, A., 2004. Ankle and subtalar kinematics measured with intracortical pins during the stance phase of walking. Foot Ankle Int. 25, 357–364.
Arndt, A., Wolf, P., Nester, C., Liu, A., Jones, R., Howard, D., Stacoff, A., Lundgren, P., Lundberg, A., 2006. Intrinsic foot motion measured in vivo during barefoot running. J. Biomech. 39, S182.
Baker, R., 2003. Letter to the editor: ISB recommendation on definition of joint coordinate systems for the reporting of human joint motion—part I: ankle, hip and spine. J. Biomech. 36 (2), 300–302.
Bartlett, R., 2007. Introduction to sports biomechanics: analysing human movement patterns. Routledge, Abingdon, England.
Barnett, G.H., Napier, J.R., 1952. The axis of rotation at the ankle joint in man. Its influence upon the form of the talus and the mobility of the Fibula. J. Anat. Lond. 86, 1–9.
Cignoni, P., Callieri, M., Corsini, M., Dellepiane, M., Ganovelli, F., Ranzuglia, G., 2008. Meshlab: an open-source mesh processing tool. Eurographics Italian Chapter Conference.
Correa, T.A., Pandy, M.G., 2011. A mass-length scaling law for modelling muscle strength in the lower limb. J. Biomech. 44 (16), 2782–2789.
Delp, S.L., Loan, J.P., Hoy, M.G., Zajac, F.E., Topp, E.L., Rosen, J.M., 1990. An interactive graphics-based model of the lower extremity to study orthopaedic surgical procedures. IEEE Trans. Biomed. Eng. 37, 757–767.
Delp, S.L., Anderson, F.C., Arnold, A.S., Loan, P., Habib, A., John, C.T., Guendelman, E., Thelen, D.G., 2007. OpenSim: open-source software to create and analyze dynamic simulations of movement. IEEE Trans. Biomed. Eng. 54, 1940–1950.
Dettwylera, M., Stacoffa, A., Kramers-de Quervaina, I.A., Stüssia, E., 2004. Modelling of the ankle joint complex. Reflections with regards to ankle prostheses. Foot Ankle Surg. 10, 109–119.
Di Marco, R., Rossi, S., Racic, V., Cappa, P., Mazzà, C., 2016. Concurrent repeatability and reproducibility analyses of four marker placement protocols for the foot-ankle complex. J. Biomech. 49, 3168–3176.
Di Marco, R., Scalona, E., Pacilli, A., Cappa, P., Mazzà, C., Rossi, S., 2018. How to choose and interpret similarity indices to quantify the variability in gait joint kinematics. Int. Biomech 5 (1), 1–8.
Dul, J., Johnson, G.E., 1985. A kinematic model of the ankle joint. J Biomed Eng. 7, 137–143.
Durkin, J.L., Dowling, J.J., 2006. Body segment parameter estimation of the human lower leg using an elliptical model with validation from DEXA. Ann. Biomed. Eng. 34, 1483–1493.
Evans, A., 2010. Paediatrics. The Pocket Podiatry Guide. Churchill Livingstone Elsevier.
Esbjörnsson, A.C., Iversen, M.D., André, M., Hagelberg, S., Schwartz, M.H., Broström, E.W., 2015. Effect of intraarticular corticosteroid foot injections on walking function in children with juvenile idiopathic arthritis. Arthritis Care Res. 67 (12), 1693–1701.
Fick, R., 1911. Handbuch der Anatomie und Mechanik der Gelenke: III, Spezielle Gelenk-und Muskelmechanik. Gustav Fischer Verlag, Jena.
Hannah, I., Montefiori, E., Modenese, L., Prinold, J., Viceconti, M., Mazzà, C., 2017. Sensitivity of a juvenile subject-specific musculoskeletal model of the ankle joint to the variability of operator-dependent input. Proc. Inst. Mech. Eng. [H] 231, 415–422.
Hicks, J.H., 1953. The mechanics of the foot: the joints. J. Anat. 87, 345–357.
Hicks, J., Uchida, T., Seth, A., Rajagopal, A., Delp, S.L., 2015. Is my model good enough? Best practices for verification and validation of musculoskeletal models and simulations of human movement. J. Biomech. Eng. 137 (2), 020905.
Inman, V.T., 1976. The Joints of the Ankle. Williams and Wilkins, Baltimore.
Isman, R.E., Inman, V.T., 1969. Anthropometric studies of the human foot and ankle. Bullet. Prosthet. Res. 10 (11), 97–129.
Lamberto, G., Martelli, S., Cappozzo, A., Mazzà, C., 2017. To what extent is joint and muscle mechanics predicted by musculoskeletal models sensitive to soft tissue artefacts. J. Biomech. 62, 68–76.
Leitch, J., Stebbins, J., Zavatsky, A.B., 2010. Subject-specific axes of the ankle joint complex. J. Biomech. 43, 2923–2928.
Lewis, G.S., Cohen, T.L., Seisler, A.R., Kirby, K.A., Sheehan, F.T., Piazza, S.J., 2009. In vivo tests of an improved method for functional location of the subtalar joint axis. J. Biomech. 42, 146–151.
Lundberg, A., 1989. Kinematics of the ankle and foot: in vivo roentgen stereophotogrammetry. Ph.D. Thesis, Deptartment of Orthopaedics, Karolinska Hospital, Stolkholm, Sweden. Acta Orthopaedica Scandinavia 60 (Suppl), 233.
Manter, J.T., 1941. Movements of the subtalar and transverse tarsal joints. Anatomic. Record 80, 397.
Malaquias, T.M., Silveira, C., Aerts, W., De Groote, F., Dereymaeker, G., Vander Sloten, J., Jonkers, I., 2017. Extended foot-ankle musculoskeletal models for application in movement analysis. Comput. Methods Biomech. Biomed. Eng. 20 (2), 153–159.
Malattia, C., Damasio, M.B., Pistorio, A., Ioseliani, M., Vilca, I., Valle, M., Ruperto, N., Viola, S., Buoncompagni, A., Magnano, G.M., Ravelli, A., Tomà, P., Martini, A., 2011. Development and preliminary validation of a paediatric-targeted MRI scoring system for the assessment of disease activity and damage in juvenile idiopathic arthritis. Ann. Rheum. Dis. 70, 440–446.
Mattingly, B., Talwalkar, V., Tylkowski, C., Stevens, D.B., Hardy, P.A., Pienkowski, D., 2006. Three-dimensional in vivo motion of adult hind foot bones. J. Biomech. 39 (4), 726–733.
Modenese, L., Montefiori, E., Wang, A., Wesarg, S., Viceconti, M., Mazzà, C., 2018. Investigation of the dependence of joint contact forces on musculotendon parameters using a codified workflow for image-based modelling. J. Biomech. 73, 108–118.
Nichols, T.E., Holmes, A.P., 2002. Nonparametric permutation tests for functional neuroimaging: a primer with examples. Hum. Brain Mapp. 15 (1), 1–25.
Nusman, C.M., Ording Muller, L.S., Hemke, R., Doria, A.S., Avenarius, D., Tzaribachev, N., et al., 2016. Current status of efforts on standardizing magnetic resonance imaging of Juvenile idiopathic arthritis: Report from the OMERACT MRI in JIA Working Group and Health-e-Child. J. Rheumatol. 43, 239–244.
Ostergaard, M., Peterfy, C., Conaghan, P., McQueen, F., Bird, P., Ejbjerg, B., et al., 2003. OMERACT rheumatoid arthritis magnetic resonance imaging studies. Core set of

MRI acquisitions, joint pathology definitions, and the OMERACT RA-MRI scoring system. J. Rheumatol. 30, 1385–1386.
Parr, W.C.H., Chatterjee, H.J., Soligo, C., 2012. Calculating the axes of rotation for the subtalar and talocrural joint using 3D bone reconstructions. J. Biomech. 45, 1103–1107.
Pataky, T.C., 2012. One-dimensional statistical parametric mapping in Python. Comput. Methods Biomech. Biomed. Eng. 15, 295–301.
Prinold, J.I., Mazzà, C., Di Marco, R., Hannah, I., Malattia, C., Magni-Manzoni, S., Petrarca, M., Ronchetti, A., Tanturri de Horatio, L., van Dijkhuizen, E.H.P., Wesarg, S., Viceconti, M., 2016. A patient-specific foot model for the estimate of ankle joint forces in patients with juvenile idiopathic arthritis. Ann. Biomed. Eng. 44, 247–257.
Rasmussen, O., Tovborg-Jensen, I., 1982. Mobility of the ankle joint: recording of rotator movements in the talocrural joint in vitro with and without the lateral collateral ligaments of the ankle. Acta Orthop. Scand. 53, 155–160.
Ravelli, A., Martini, A., 2007. Juvenile idiopathic arthritis. Lancet 369 (9563), 767–778.
Roaas, A., Anderson, G.B., 1982. Normal range of motion of the hip, knee and ankle joints in male subjects, 30–40 years of age. Acta Orthop. Scand. 53 (2), 205–208.
Roach, K.E., Wang, B., Kapron, A.L., Fiorentino, N.M., Saltzman, C.L., Foreman, K.B., Anderson, A.E. In, 2016. Vivo kinematics of the tibiotalar and subtalar joints in asymptomatic subjects: a high-speed dual fluoroscopy study. ASME. J. Biomech. Eng. 138 (9), pp. 091006–091006-9.
Saraswat, P., Andersen, M.S., MacWilliams, B.A., 2010. A musculoskeletal foot model for clinical gait analysis. J. Biomech. 43 (9), 1645–1652.
Scheys, L., Loeckx, D., Spaepen, A., Suetens, P., Jonkers, I., 2009. Atlas-based non-rigid image registration to automatically define line-of-action muscle models: a validation study. J. Biomech. 42, 565–572.
Scott, S.H., Winter, D.A., 1991. Talocrural and talocalcaneal joint kinematics and kinetics during the stance phase of walking. J. Biomech. 24, 743–752.
Sepic, S.B., Murray, M.P., Mollinger, L.A., Spurr, G.B., Gardner, G.M., 1986. Strength and range of motion in the ankle in two age groups of men and women. Am. J. Phys. Med. 65, 75–84.
Siegler, S., Chen, J., Schneck, C.D., 1988. The three-dimensional kinematics and flexibility characteristics of the human ankle and subtalar joints. Part 1: kinematics. J. Biomech. Eng. 110, 364–373.
Siegler, S., Toy, J., Seale, D., Pedowitz, D., 2014. The clinical biomechanics award 2013 – presented by the international society of biomechanics: new observations on the morphology of the talar dome and its relationship to ankle kinematics. Clin. Biomech. 29 (1), 1–6.
Stebbins, J., Harrington, M., Thompson, N., Zavatsky, A., Theologis, T., 2006. Repeatability of a model for measuring multi-segment foot kinematics in children. Gait & Posture 23, 401–410.
Steger, S., Kirschner, M., Wesarg, S., 2012. Articulated atlas for segmentation of the skeleton from head & neck CT datasets. In: 9th IEEE International Symposium on Biomedical Imaging (ISBI). Barcelona, Spain.
Valente, G., Crimi, G., Vanella, N., Schileo, E., Taddei, F., 2017. nmsBuilder: Freeware to create subject-specific musculoskeletal models for OpenSim. Comput. Methods Programs Biomed. 152, 85–92.
van den Bogert, A.J., Smith, G.D., Nigg, B.M., 1994. In vivo determination of the anatomical axes of the ankle joint complex: an optimization approach. J. Biomech. 27, 1477–1488.
van Langelaan, E.J., 1983. A kinematical analysis of the tarsal joints. An X-ray photogram-metric study. Ph.D. Thesis. Acta Orthopaedica Scandinavia 54 (Suppl), 204.
Vicon Motion Systems, L., 2012. Biomechanical Research, 2012. http://www.irc-web.co.jp/vicon_web/news_bn/PIGManualver1.pdf.
Westblad, P., Hashimoto, T., Winson, I., Lundberg, A., Arndt, A., 2002. Differences in ankle-joint complex motion during the stance phase of walking as measured by superficial and bone-anchored markers. Foot Ankle Int. 23 (9), 856–863.
Woltring, H.J., 1986. A FORTAN package for generalized cross-validatory spline smoothing and differentiation. Adv. Eng. Softw. 8 (2), 104–113.